COMMUNICATION

ADVANCED
MATERIALS
INTERFACES

www.advmatinterfaces.de

Check for updates

A Facile Fabrication and Transfer Method of Vertically Aligned Carbon Nanotubes on a Mo/Ni Bilayer for Wearable Energy Devices

Chanhyuk Lim, Yoonsoo Shin, Seungki Hong, Sangkyu Lee,* and Dae-Hyeong Kim*

Carbon nanotubes are a promising material for flexible/wearable electrochemical device due to their mechanical softness, chemical stability, and high conductivity. Furthermore, the vertically aligned form of carbon nanotubes (VACNTs) have a large surface area due to their unique three-dimensional (3D) nanostructure. Thus, VACNTs are particularly useful for wearable electrochemical sensors and/or energy devices. However, VACNTs are generally grown via a high-temperature chemical vapor deposition process, which requires a rigid substrate. As a flexible/wearable device platform, therefore, VACNTs should be transferred from rigid substrates to soft substrates. Here, a facile fabrication and transfer method of a unique 3D nanostructure, that is, VACNTs on the Mo/Ni bilayer, for high performance flexible/wearable devices is reported. After growth of VACNTs on a Mo/Ni bilayer, VACNTs with the Mo/Ni bilayer can be easily peeled-off from the SiO_2 wafer by using weak adhesion of Ni to SiO_2 for transfer printing onto polymeric/elastomeric substrates. Moreover, the Mo layer helps facile growth of VACNTs, and the Mo/Ni bilayer underneath VACNTs maximizes the lateral current flow. The proposed 3D nanostructure (VACNTs on the Mo/Ni bilayer) is successfully applied as flexible electrodes for high-performance wearable asymmetric supercapacitors.

Carbon nanotubes (CNTs) have been used as a key material for flexible electronic/electrochemical devices,[1] because they are electrically conductive, mechanically deformable, and chemically stable.[2] In particular, they have a large surface area and thereby exhibit high electrochemical activity, which have enabled various applications in electrochemical sensors,[3] actuators,[4] and energy storage devices.[5,6] For device fabrication, conventional CNTs are usually processed as a dispersed solution[7,8] and coated on various substrates using diverse methods such as the immersion,[9,10] drop-casting,[11] spin-coating,[12] and filtration.[13] Also, CNTs can be mixed with polymeric/elastomeric

Dr. C. Lim, Y. Shin, S. Hong, Dr. S. Lee, Prof. D.-H. Kim
Center for Nanoparticle Research
Institute for Basic Science (IBS)
Seoul 08826, Republic of Korea
E-mail: sangkyulee@snu.ac.kr; dkim98@snu.ac.kr
Dr. C. Lim, Y. Shin, S. Hong, Prof. D.-H. Kim
School of Chemical and Biological Engineering
Institute of Chemical Processes
Seoul National University
Seoul 08826, Republic of Korea

The ORCID identification number(s) for the author(s) of this article can be found under https://doi.org/10.1002/admi.201902170.

materials to make conductive composites which can be applied to flexible electrodes and deformable devices.[14] However, CNT films fabricated by these methods have a randomly-aligned two-dimensional (2D) structure[15] and thus have a limited surface area in comparison with 3D nanostructures.

Meanwhile, another type of CNTs, the vertically aligned carbon nanotubes (VACNTs), has attracted a large attention. They are the bundled form of CNTs vertically grown on a rigid substrate with appropriate catalyst layers. It constructs the 3D nanostructure that looks like a forest of CNTs. They have a much larger surface area than the film-shape 2D CNT networks due to their unique 3D nanostructure. The electrochemical reactions happen on the surface of CNTs, and thus this large surface area can maximize the electrochemical activity of CNTs and enable high-performance electrochemical sensor[16] and/or energy storage device applications.[17]

Such VACNTs are generally synthesized by high-temperature chemical vapor deposition (CVD) processes.[18,19] However, typical deformable substrates for wearable devices are made of polymers and/or elastomers that are vulnerable to high temperature. Therefore, in order to utilize the VACNTs to fabricate wearable devices, they should be transferred from a rigid substrate for CNT growth to a flexible substrate for device fabrication.[20] Many attempts have been made to transfer free-standing VACNT networks onto soft substrates, such as weakening the substrate-VACNT adhesion[21,22] or tearing-off VACNTs with polymers/elastomers penetrated into the VACNT forest.[23] However, these methods are difficult and requires sensitive control because very small change in the annealing condition or penetration depth of polymers/elastomers result in the low transfer yield and device performance.

In addition, the transferred VACNT network has low electrical conductivity in the lateral direction due to the weak horizontal percolation between nanotubes to form a laterally conductive pathway, despite high conductivity in the vertical direction following the vertical nanotubes. Thus further processing steps such as the lateral combing and/or metal deposition process should have been additionally applied to the transferred VACNT networks to achieve both high lateral and vertical conductivity. This is particularly critical for efficiently inject and

1902170 (1 of 8)

extract current into and from the VACNT electrodes. However, these additional processes are tricky and expensive, exhibit low yield, and increase the overall fabrication complexity. Therefore, a novel fabrication and transfer method for the VACNTs with an engineered structure for lateral conductive pathways is required for the development of high performance wearable devices.

We herein report a facile fabrication and transfer method of a unique 3D nanostructure, that is, VACNTs on the Mo/Ni bilayer, for high-performance flexible electrodes and wearable energy storage devices. The fabricated 3D nanostructure before the transfer process, that is, VACNTs synthesized on a Mo/Ni bilayer with a SiO_2 wafer as a handling substrate, is shown in **Figure 1**a. The Ni layer serves as an assisting layer for easy peel-off of the nanostructure from the SiO_2 substrate. The critical adhesion energy (G_c) of the Ni film on the SiO_2 substrate is 1.3 (J m^{-2}), while that of other metals such as Ti is much higher

(e.g., G_c of Ti is 3.5 J m^{-2}).[24] Due to this low G_c of Ni on SiO_2, the entire nanostructure on the Ni film including VACNTs can be easily peeled-off from the substrate (Figure 1b). Meanwhile, the Mo layer between VACNTs and Ni enables the facile VACNT growth via the CVD process (Figure 1c). Mo has very small interference to the catalyst layers (here, the Fe/Al catalyst layer is used) for the CVD growth of VACNTs.

Another important function of the Mo/Ni layer is to serve as an inter-VACNT horizontal current pathway, which dramatically increases conductivity of the entire 3D nanostructure in the lateral direction. In fact, despite excellent vertical conductivity of VACNTs following each vertical nanotube, low electrical conductivity into the lateral direction (i.e., conduction between nanotubes) has been a major bottleneck for VACNTs to be applied to high-performance flexible electrodes and wearable devices. But the 3D nanostructure of VACNTs with the Mo/Ni bilayer can solve this issue by adding a highly conductive lateral
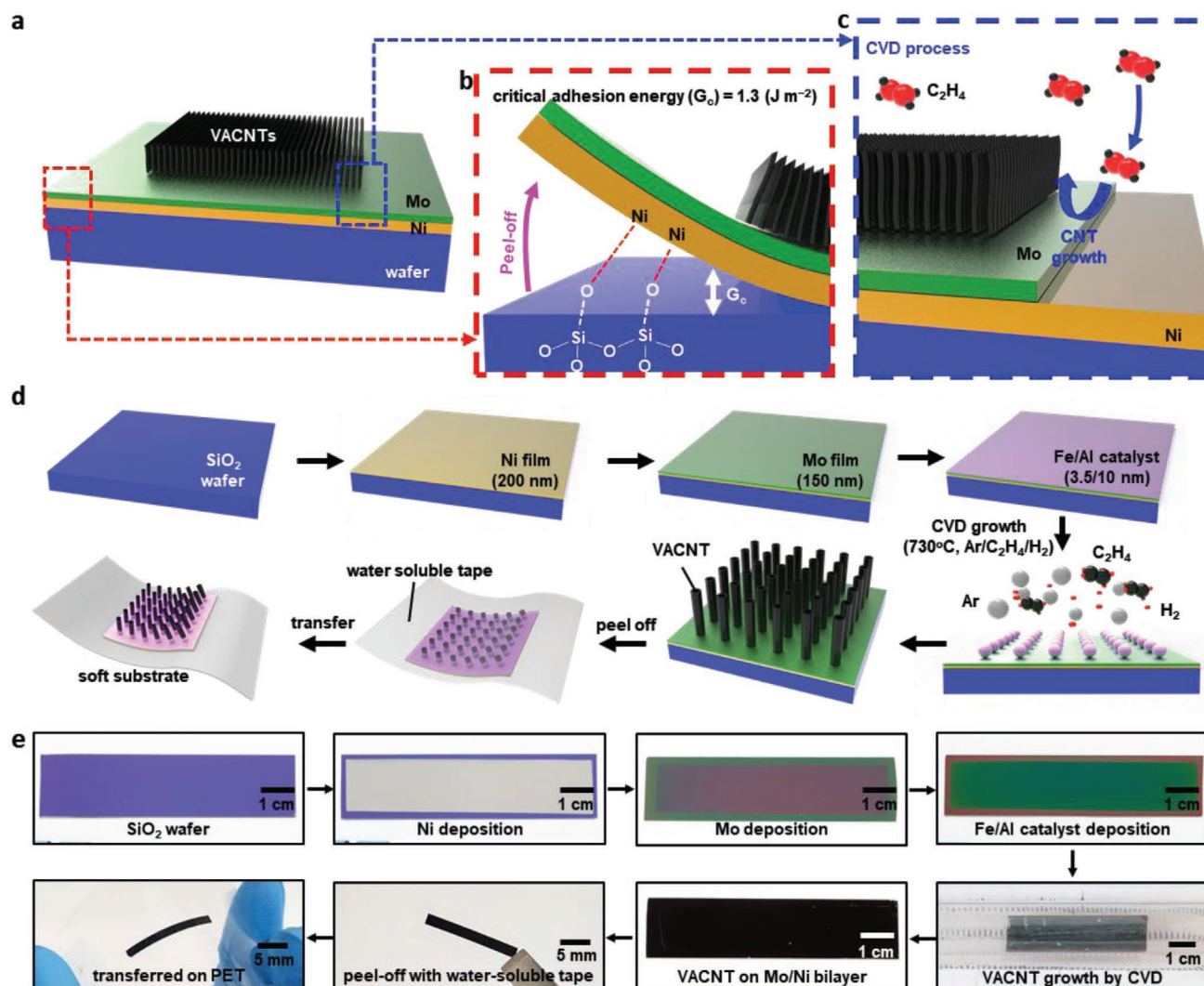

Figure 1. a) Schematic illustration of a 3D nanostructure comprised of VACNTs and a Mo/Ni bilayer on the SiO_2 substrate (wafer). b) Weak critical adhesion energy ($G_c = 1.3$ J m^{-2}) between the Ni peel-off layer and the SiO_2 substrate. c) The VACNT growth with the Fe/Al catalyst using the CVD process can be facilitated with the Mo protecting layer. d) Schematic illustrations and e) corresponding photographs that describe the fabrication and transfer procedures of the 3D nanostructure (i.e., VACNTs on a Mo/Ni bilayer).

current pathway comprised of the Mo and Ni metal bilayer film to the vertical current paths following the nanotubes.

Figure 1d,e show schematic illustrations and corresponding images for more details about the fabrication and transfer process of the VACNTs on the Mo/Ni bilayer. The Ni (200 nm) and Mo (150 nm) films were deposited on a SiO_2 wafer by e-beam evaporation and radio frequency sputtering, respectively. A thin bilayer catalyst (Fe/Al = 3.5/10 nm) for growth of VACNTs in CVD was added via thermal evaporation. The VACNTs were grown through CVD by supplying a gas mixture of ethylene, hydrogen, and argon at 730 °C under the atmospheric pressure. Once the VACNTs are successfully synthesized, a water soluble tape is applied to the VACNTs.[25] The entire 3D nanostructure (i.e., VACNTs on the Mo/Ni bilayer) can be easily detached from the substrate using a water-soluble tape due to the weak adhesion between the Ni layer and the SiO_2 substrate (Figure S1, Supporting Information), the picked-up 3D nanostructure is transferred onto a selected soft substrate, and the water soluble tape is removed.

The transferred 3D nanostructure that consists of VACNTs and the Mo/Ni bilayer has two different (i.e., vertical and lateral) conductive pathways as illustrated in **Figure 2**a. Redox reactions efficiently occur on the surface of VACNTs, which result in large electrical current, because of the CNTs' large

surface area and excellent electrochemical activity (Figure 2b). Electrons generated from the redox reactions at the surface of VACNTs can be vertically transported through the nanotubes (vertical conduction), while the electrons that reach the bottom Mo/Ni bilayer move through metal layers and eventually reach external circuits (lateral conduction) (Figure 2c). By combining these vertical and lateral conductions, highly efficient conducting pathways for the large amount of electrons generated by redox reactions can be made. Therefore, considering the intrinsically soft mechanical property of CNTs, the 3D VACNT network with the Mo/Ni bilayer, when properly transferred to the flexible substrates, can be a good choice for the fabrication of high-performance flexible electrodes and wearable electrochemical devices.[26]

The high conductivity of CNTs following the vertical nanotubes has been well studied by previous reports.[23] But, the methods to achieve high lateral conductivity between nanotubes has not been studied well. Here, we investigated the contribution of the metallic bilayer on the lateral conduction by comparing the conductance of VACNTs on the SiO_2 wafer (Figure 2d), a Mo/Ni bilayer (Figure 2e), and VACNTs on the Mo/Ni bilayer (Figure 2f). These three types of samples were patterned into a line shape, and their electrical resistances were compared (Figure 2g). The resistance of VACNTs on the SiO_2
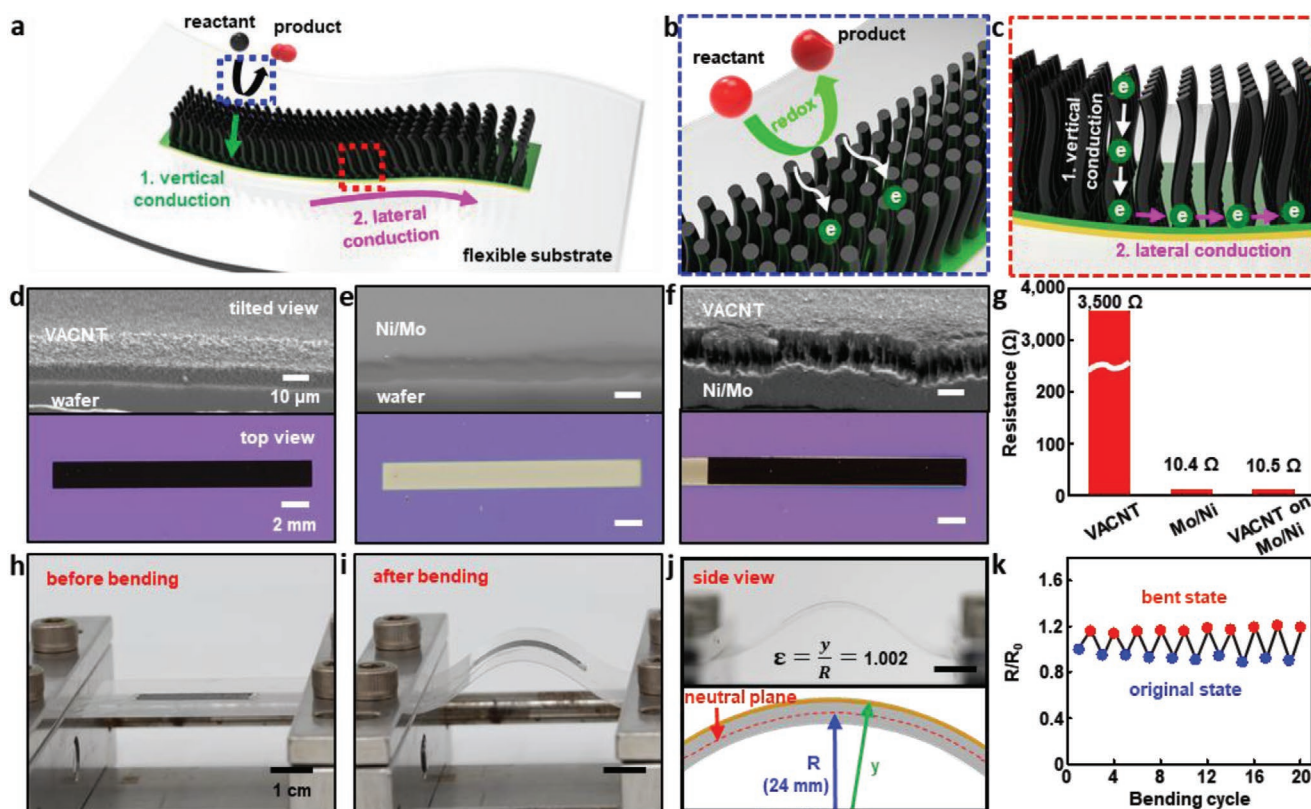

Figure 2. Schematic illustration of a) the overall 3D nanostructured electrode, b) the redox reaction on the surface of VACNTs, and c) the vertical and lateral conduction pathways. SEM images (top) and optical photographs (bottom) of d) bare VACNTs, e) a Ni/Mo film, and f) VACNTs grown on a Ni/Mo bilayer. g) Comparison of the electrical resistance of three types of electrodes, that is, bare VACNTs, a Ni/Mo film, and VACNTs on a Ni/Mo bilayer. Optical image of VACNTs on the Ni/Mo bilayer transferred onto a PET film h) before and i) after bending on the unidirectional bending stage. j) Optical image (side view; top) and schematic illustration (bottom) that shows the estimation procedure of the induced strain on the bent electrodes. k) Relative resistance change during the repetitive bending test.
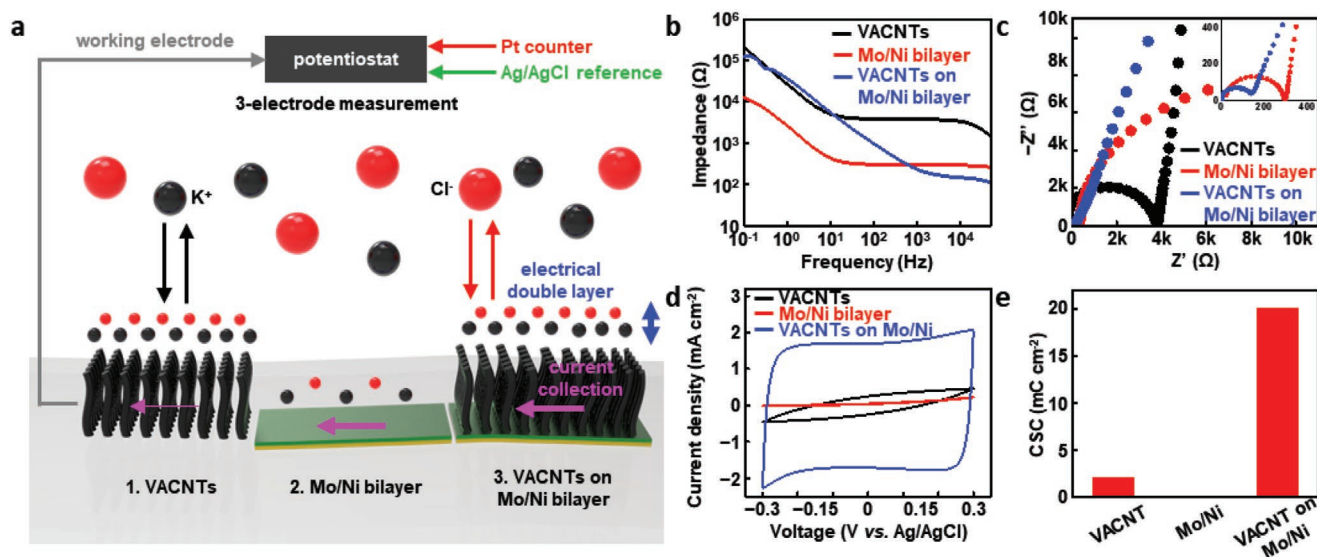
Figure 3. a) Schematic illustration that describes the measurement setup and principle of the electrochemical surface property. Comparison of AC impedance among three types of electrodes, that is, bare VACNTs, a Mo/Ni film, and VACNTs on Mo/Ni using the b) Bode plot and c) Nyquist plot. d) Cyclic voltammetry test for bare VACNTs, a Mo/Ni film, and VACNTs on Mo/Ni at a scan rate of 100 mV s^{-1} in the 0.1 M KCl solution and e) the calculated charge storage capacities for three electrodes.

wafer was highest (3500 Ω) among all three types of electrodes. On the other hand, the Mo/Ni bilayer and the VACNTs on the Mo/Ni film have similar level of resistance, 10.5 Ω, which reveals that the major lateral conduction is based on the Mo/Ni layer.

When VACNTs with the metal bilayer are transferred onto flexible or stretchable substrates such as the polyethylene terephthalate (PET) or poly(dimethylsiloxane) (PDMS) substrate, they become deformable. A line-shaped VACNT pattern was prepared and transferred onto the adhesive-coated PET substrate to test the mechanical stability under repetitive bending (Figure 2h,i). When the PET is bent, the patterned 3D nanostructure is also deformed with the induced strain of ε (Figure 2j). The induced strain can be calculated using the following equation.

$$\varepsilon = r/R \tag{1}$$

where r is the bending radius at the electrode surface and R is the bending radius of the neutral plane that is the position where strain is zero. Here, the bending radius of the neutral plane is observed as ≈24 mm, and the distance between the electrode surface and the neutral plane can be approximated to be ≈0.05 mm that is a half of the thickness of PET substrate. The calculated strain is ≈0.2%, and the resistance is maintained stable during the cyclic bending test (Figure 2k). When they are combined with appropriate structures or patterns, such as the buckled wavy structure,[27,28] serpentine patterns,[29] or microcracked film structure,[30] they can become stretchable.[31,32]

In addition to the unique vertical and lateral electrical conduction of the VACNTs on the Mo/Ni bilayer, the key advantage of the nanostructure is that they are electrochemically active and chemically stable. The VACNTs form an electric double layer in an ionic solution stably.[33] Also, the 3D nanostructure of VACNTs has a much larger surface area than the 2D random

CNT networks fabricated by solution processes. For these reasons, VACNTs on the Mo/Ni bilayer could be a good candidate for the flexible electrodes of the high-performance electrochemical devices such as wearable supercapacitors.

To investigate the electrochemical performance of the developed 3D-nanostructure-based flexible electrodes, electrochemical properties such as impedance under the alternative current (AC) mode or charge storage capacity in the ionic solution were characterized. First, the AC impedance of VACNTs, a Mo/Ni bilayer film, and VACNTs on the Mo/Ni bilayer were separately measured in an aqueous electrolyte solution containing 0.1 M KCl over the frequency range of 10^{-1}–10^5 Hz via the three-electrode-type measurement (working, Pt counter, and Ag/AgCl reference electrode) (**Figure 3**a). These three types of electrodes (i.e., VACNTs, Mo/Ni bilayer, and VACNTs on a Mo/Ni bilayer) were patterned as a line shape similar to those shown in Figure 2.

The Bode plots in Figure 3b show the characteristic impedance tendency of each electrode. The VACNTs and the VACNTs on the Mo/Ni bilayer show the similar level of impedance in the low frequency region. As the frequency increases, the impedance of the VACNTs on the Mo/Ni bilayer becomes the lowest among three electrodes. Furthermore, Nyquist plots in Figure 3c show that the VACNTs on the Mo/Ni bilayer show the smallest radius of the hemisphere among three curves, which means that the resistance related to the charge transfer is lower than other types of electrodes. These results are due to the combination of the facile vertical and lateral conduction.

To estimate the charge storage capacity of the electrodes in an ionic solution, cyclic voltammetry (CV) measurements were also performed for each electrode in the 0.1 M KCl aqueous solution (Figure 3d). The area under the CV curve indicates the adsorption capability of the ions on the surface of each electrode, which is also called as the charge storage capacity (CSC) of the electrode.[34] The calculated CSC for each electrode is compared
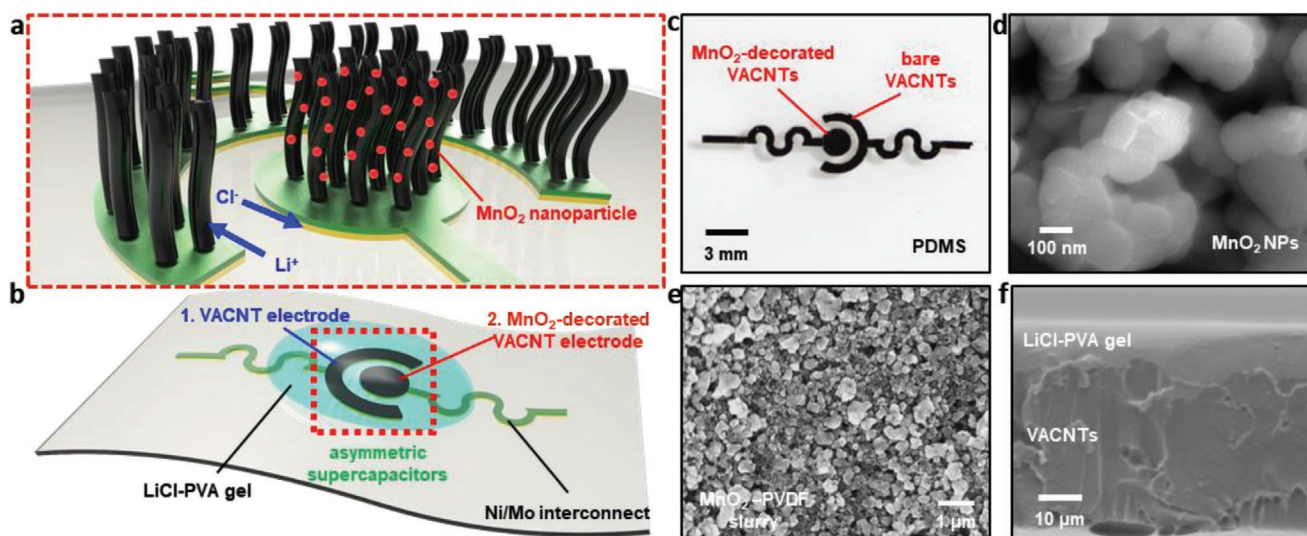
**ADVANCED
SCIENCE NEWS**
www.advancedsciencenews.com

**ADVANCED
MATERIALS
INTERFACES**
www.advmatinterfaces.de

Figure 4. a) Schematic illustration for the magnified view of the asymmetric supercapacitor. b) Schematic illustration of the asymmetric supercapacitor comprised of a VACNTs on Mo/Ni bilayer and MnO$_2$-decorated VACNTs on Mo/Ni bilayer. c) Optical image of the fabricated supercapacitor on the PDMS substrate. SEM images of d) the synthesized MnO$_2$ nanoparticles, e) the MnO$_2$ layer on the VACNTs, and f) the cross-sectional view of the gel electrolyte-infiltrated VACNTs.

in Figure 3e; 2.04 μC mm^{-2} for VACNTs, 0.06 μC mm^{-2} for the Mo/Ni bilayer, and 20.09 μC mm^{-2} for VACNTs on the Mo/Ni bilayer. The electrode made of VACNTs on the Mo/Ni bilayer exhibited much higher CSC than the VACNTs or Mo/Ni bilayer electrode.

By utilizing the developed 3D nanostructured electrode, we demonstrated the fabrication of a deformable asymmetric supercapacitor. **Figure 4**a shows a schematic illustration describing the structure of the asymmetric supercapacitor by using the proposed 3D nanostructured electrode based on the VACNTs with a Mo/Ni bilayer. One electrode is the bare VACNTs/metal-bilayer electrode, while the other electrode is the VACNTs/metal-bilayer electrode decorated with MnO$_2$ nanoparticles. MnO$_2$ was chosen as a model material in this demonstration because it is a representative supercapacitor material with high capacitance.[35–37] By combining the bare VACNTs/metal-bilayer electrode with the MnO$_2$-decorated VACNTs/metal-bilayer electrode, an asymmetric supercapacitor was constructed (Figure 4b). Figure 4c shows the image of the fabricated supercapacitor transferred onto the PDMS substrate. The MnO$_2$ nanoparticles (<200 nm) were synthesized by the reduction of KMnO$_4$ in the presence of ethylene glycol (Figure 4d),[38] and they were mixed with carbon black and poly(vinylidene fluoride-co-hexafluoropropylene) (PVdF-HFP) in a N-methyl-2-pyrrolidone solvent to make the MnO$_2$ slurry. The MnO$_2$ slurry was coated on the VACNT electrode by drop-casting (Figure 4e).

A gel electrolyte comprised of LiCl and poly(vinyl alcohol) (PVA) was used as a solid electrolyte for the asymmetric supercapacitor. The LiCl–PVA gel electrolyte penetrates well inside the VACNT networks (Figure 4f). It is attributed to the high free volume of the VACNT forest.[39] Its hygroscopic property and mechanically flexibility are very helpful to make the supercapacitor as a wearable form. Furthermore, the use of the LiCl–PVA gel as a solid-state electrolyte, instead of using the liquid-type electrolyte, is important for the wearable device

application.[40] In addition, the operation voltage of the aqueous electrolyte can be up to twice as high as that of electric double layer capacitors or pseudo-capacitors, which enables the fabrication of high energy density supercapacitors compared to symmetric supercapacitors.

CV tests for the VACNTs/metal-bilayer electrode and the MnO$_2$-decorated VACNTs/metal-bilayer electrode were conducted in 1 M Na$_2$SO$_4$ aqueous solution using a three-electrode system. The CV curve of the VACNTs/metal-bilayer electrode was obtained in the voltage range of –1 to 0 V, and the MnO$_2$-decorated VACNTs/metal-bilayer electrode was cycled in the voltage range of 0 to 0.8 V (**Figure 5**a). The full cell comprised of these electrodes was cycled in the voltage range of 0 to 1.8 V and the obtained CV curves are summarized in Figure 5b. The galvanostatic charge–discharge tests were also performed under various current densities in the same voltage window (Figure 5c). The areal capacitance of the full cell was 8 mF cm^{-2} at the current density of 0.1 mA cm^{-2} and 5 mF cm^{-2} at a high current density of 5 mA cm^{-2}. The areal energy density and power density of the asymmetric supercapacitor were also calculated using the result of Figure 5c. The results are summarized as a Ragone plot (Figure S2, Supporting Information). Finally, the cycle performance of the full cell was calculated from the CV results obtained at a scan rate of 1000 mV s^{-1} as shown in Figure 5d. The areal capacitance of the full cell was ≈4.6 mF cm^{-2} at the first cycle, and the capacitance of ≈4.2 mF cm^{-2} was obtained even after 1000 cycles.

Although the asymmetric supercapacitors can provide the large energy density based on the large operating potential window, there is also a demand for better performance depending on the system applications over the single cell performance. For example, energy-requiring devices such as stretchable skin patch,[41,42] artificial sensory system,[43] stretchable sensor system,[44] and biosignal monitoring system[45] need a higher amount of power supply. In such cases, two
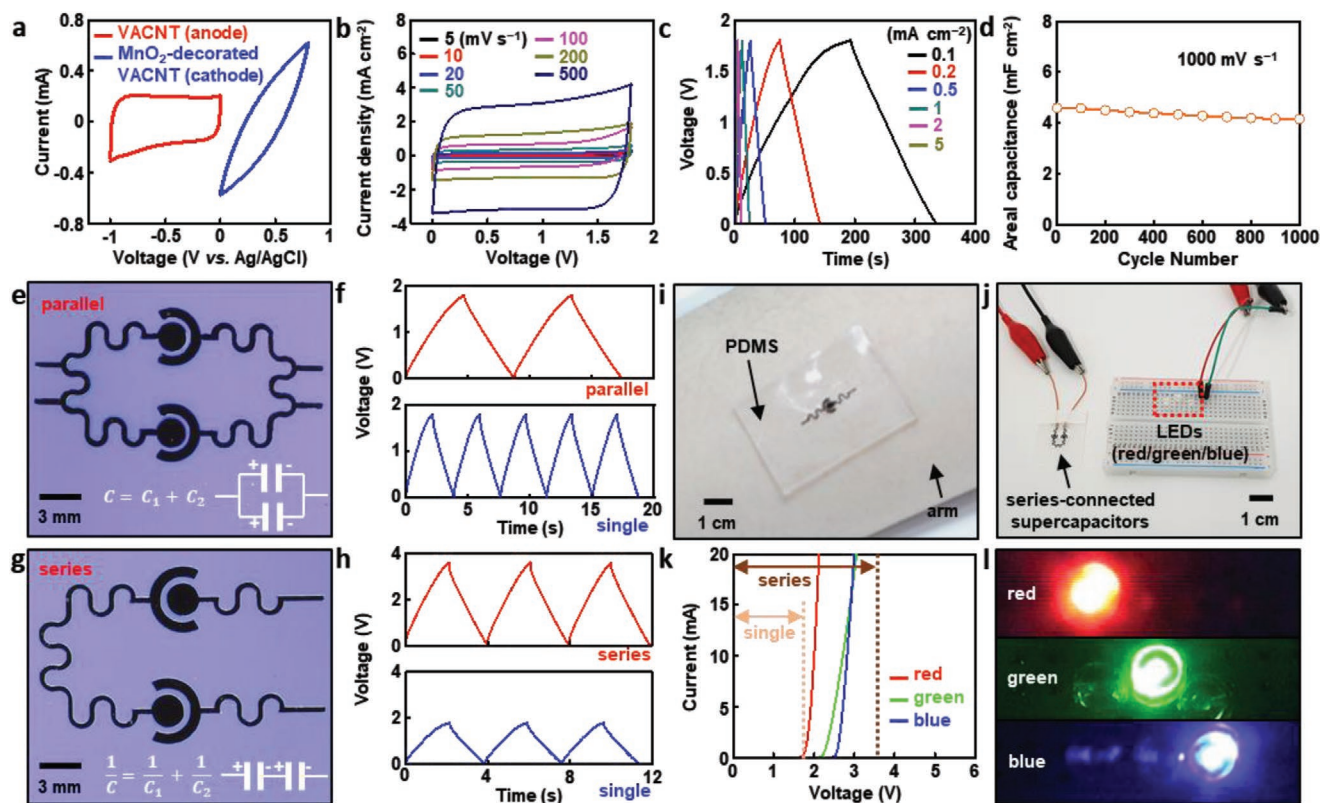
Figure 5. a) CV curves of the VACNT/metal-bilayer electrode and the MnO₂-decorated VACNT/metal-bilayer electrode at a scan rate of 200 mV s⁻¹. b) CV curves of the asymmetric capacitors comprised of the VACNT/metal-bilayer electrode and the MnO₂-decorated VACNT/metal-bilayer electrode at various scan rates. c) Galvanostatic charge–discharge curves of the asymmetric supercapacitors at various current densities. d) Cycle performance of the asymmetric supercapacitor calculated from the CV results at the scan rate of 1000 mV s⁻¹. e) Image of two supercapacitor cells connected in parallel and f) its galvanic charge–discharge cycle test results. g) Image of two supercapacitor cells connected in series and h) its galvanic charge–discharge cycle test results. i) Image of the supercapacitor transferred on the human skin using the PDMS substrate. j) Image of series-connected supercapacitors wired with three colors of LEDs (red, green, and blue) k) I–V curves of red, green, and white LEDs. l) Image of LEDs turned on by using the series-connected supercapacitors.

(or multiple) single supercapacitor cells can be connected in parallel or series. The parallel connection shown as Figure 5e increases the capacity (Figure 5f), while the series connection in Figure 5g doubles the maximum potential (Figure 5h).

Additionally, the asymmetric supercapacitors on soft substrates are highly deformable (Figure S3, Supporting Information) and thus they can be conformally attached on the human body to be utilized as an energy-supplying device for the wearable electronic system. The supercapacitors with the series connection, as an example, is transferred on the human skin with the PDMS substrate (Figure 5i). Three types of light emitting diodes (LEDs) (i.e., red, green, and blue) are used for the demonstration of the series-connected supercapacitors (Figure 5j). Each LED has a turn-on voltage between 1.8–2.6 V that is higher than the output potential of the single-cell supercapacitors, but lower than that of the series-connected double-cell supercapacitors (Figure 5k). Therefore, all types of LEDs are successfully turned on by using the series-connected supercapacitors (Figure 5l).

In summary, VACNTs are 3D CNT networks that are mechanically deformable and electrochemically active as well as have a large surface area. For this reason, VACNTs have been suggested as a promising electrode material for the high

performance deformable electrochemical devices. However, the synthesis of VACNTs directly on polymeric substrates has been limited due to the high growth temperature of VACNTs. Also the lateral conductance of VACNTs has been low, despite the high vertical conductance following the nanotubes. In this work, we proposed a facile fabrication and transfer method of VACNTs on a Mo/Ni bilayer by peeling off the underlying Ni film from a SiO₂ substrate and subsequently transferring them onto flexible substrates. Additionally, the Mo layer ensures the high quality synthesis of VACNTs. The VACNTs on the Mo/Ni bilayer showed high vertical and lateral electrical conductivity due to the VACNTs and the underlying metal bilayer, respectively.

The 3D nanostructured flexible electrodes were utilized to fabricate wearable asymmetric supercapacitors. The asymmetric supercapacitors consisted of a VACNT/metal-bilayer electrode and a MnO₂ nanoparticles-decorated VACNT/metal-bilayer electrode. The LiCl–PVA gel-based solid electrolyte replaced the conventional liquid electrolyte and thus enabled a wearable form of the asymmetric supercapacitors. In addition, larger capacity and higher output voltage were achieved by connecting two single cells in parallel or series. The fabrication and transfer method of the 3D nanostructure (i.e., VACNTs on

**ADVANCED
SCIENCE NEWS**

www.advancedsciencenews.com

**ADVANCED
MATERIALS
INTERFACES**

www.advmatinterfaces.de

a Mo/Ni bilayer) and the demonstration of the 3D nanostructure-based deformable energy storage device showed the possibility for the application of VACNTs to more diverse wearable systems.[46] Further works such as the patterned encapsulation and stretchable device fabrications are expected to enable more complex device development and system integration.[47,48]

Experimental Section

Fabrication of 3D Nanostructure: A Ni layer with a thickness of 200 nm was formed on a SiO_2 wafer with an e-beam evaporator, followed by the deposition of 150 nm thick Mo layer by radio frequency magnetron sputtering. A bilayer catalyst (Fe/Al = 3.5/10 nm) was deposited onto the Mo/Ni-deposited SiO_2 wafer via thermal evaporation. The wafer was loaded in a 1-inch quartz tube and the quartz tube was flushed with an argon flow of 300 sccm for 30 min prior to the synthesis of VACNTs. The temperature was increased to 730 °C under a flow of argon (100 sccm) and hydrogen (100 sccm). When it reached the target temperature, ethylene (75 sccm) was supplied as a carbon source for 3 min. After the synthesis of VACNTs, the quartz tube was rapidly cooled down to room temperature with a flow of argon and hydrogen.

Transfer Method: A water soluble tape (Water-Soluble Waver Solder Tape 5414, 3M, USA) was attached onto the surface of VACNTs on Mo/Ni bilayer-deposited SiO_2 wafer. The whole layers were slowly detached from the SiO_2 wafer and attached onto an adhesion-coated PET substrate or a PDMS substrate. The PDMS substrate was prepared by mixing monomer and curing agent (Sylgard 184, Dow Corning, USA) with a mixing ratio of 10:1. The sample was submerged in a de-ionized water bath to release the water soluble tape. Finally, the transferred VACNTs on Mo/Ni bilayer were dried at 60 °C in an oven for 30 min.

Fabrication of Supercapacitors: MnO_2 nanoparticles (<200 nm) were synthesized by mixing aqueous $KMnO_4$ solution (ACS reagent, Sigma-Aldrich, USA) with concentrated H_2SO_4 and ethylene glycol.[38] The slurry of MnO_2 nanoparticles was prepared by homogenizing MnO_2 nanoparticles, carbon black (Super P, Alfa Aesar, USA), and PVdF-HFP (Kynar 2801, Arkema Inc., USA) in N-methyl-2-pyrrolidone (99%, Sigma-Aldrich, USA) in a mass ratio of 80:10:10. The slurry was drop-casted on the top surface of VACNT forest and dried at 80 °C in an oven for 12 h. The gel electrolyte consisting of LiCl and PVA was prepared by dissolving 1 g of LiCl (Samchun Pure Chemical, Republic of Korea) and 1 g of PVA (Mw 89 000–98 000, 99+% hydrolyzed, Sigma-Aldrich, USA) in 10 mL of de-ionized water. The mixture was dissolved at 90 °C for 3 h and cooled down to room temperature. The prepared LiCl–PVA gel was drop-casted on the electrodes of supercapacitors and the sample was placed in a vacuum for 5 min for the complete penetration of gel into the VACNT forest. Then, it was dried at 80 °C in an oven for 1 h to prepare solid-state supercapacitors.

Characterization: The microstructure of VACNT electrodes was observed with a scanning electron microscope (SEM, S4700, Hitachi, Japan). The particle size and morphology of MnO_2 nanoparticles were characterized by using a field emission SEM (FE-SEM, JSM 4700F, JEOL, Japan). The electrical properties of the electrodes were evaluated with a digital multimeter (Fluke 179, Fluke Co., USA). To evaluate the electrochemical performance of the electrodes, cyclic voltammetry, galvanostatic charge/discharge tests, and electrochemical impedance spectroscopy measurements were conducted with a potentiostat/galvanostat (660E Potentiostat/Galvanostat, CH Instruments, USA). The areal capacitance was calculated from the results of galvanostatic charge–discharge tests by using the following equation.

$$C_{(areal, galvanostatic)} = \frac{i\Delta t}{A\Delta V} \tag{2}$$

where i is the constant current, Δt is the time interval for the voltage change ΔV, and A is the area of the electrodes. The areal capacitance was also calculated with the results of CV according to the following equation.

$$C_{(areal, cyclic\ voltammetry)} = \frac{1}{2vS\Delta V}\int I(V)\,dV \tag{3}$$

where v is the scan rate, S is the total area of the electrodes, ΔV is the applied voltage, and $I(V)$ is the voltammetric current. The areal energy density and power density of the asymmetric supercapacitor were calculated with the results of Figure 5c using the following equations.

$$E_{(areal, energy\ density)} = C \times \Delta V^2 \tag{4}$$

where C is the areal capacitance of the supercapacitor and ΔV is the potential window.

$$P_{(areal, power\ density)} = i \times \Delta V/A \tag{5}$$

where i is the discharge current, ΔV is the potential window, and A is the area of the electrodes.

Supporting Information

Supporting Information is available from the Wiley Online Library or from the author.

Acknowledgements

Conflict of Interest

The authors declare no conflict of interest.

Author Contributions

C.L. and Y.S. equally contributed to this work. C.L., S.L., and D.-H.K. designed the experiments. C.L., Y.S., and S.L. carried out the experiments and analysis. S.H. carried out the analysis of supercapacitor performance. C.L., S.L., and D.-H.K. wrote the paper. D.-H.K. and S.L. are corresponding authors of this work.

Keywords

[1] D. Son, J. H. Koo, J.-K. Song, J. Kim, M. Lee, H. J. Shim, M. Park, M. Lee, J. H. Kim, D.-H. Kim, *ACS Nano* **2015**, *9*, 5585.

[2] D. Janas, K. Z. Milowska, P. D. Bristowe, K. K. K. Koziol, *Nanoscale* **2017**, *9*, 3212.

[3] M. K. Choi, I. Park, D. C. Kim, E. Joh, O. K. Park, J. Kim, M. Kim, C. Choi, J. Yang, K. W. Cho, J.-H. Hwang, J.-M. Nam, T. Hyeon, J. H. Kim, D.-H. Kim, *Adv. Funct. Mater.* **2015**, *25*, 7109.

[4] Y.-J. Huang, H.-C. Wu, N.-H. Tai, T.-W. Wang, *Small* **2012**, *8*, 2869.

[5] C. Zhang, H. Li, A. Huang, Q. Zhang, K. Rui, H. Lin, G. Sun, J. Zhu, H. Peng, W. Huang, *Small* **2019**, *15*, 1805493.

**ADVANCED
SCIENCE NEWS**

www.advancedsciencenews.com

**ADVANCED
MATERIALS
INTERFACES**

www.advmatinterfaces.de

[6] J.-K. Kim, Y. Kim, S. Park, H. Ko, Y. Kim, *Energy Environ. Sci.* **2016**, *9*, 1264.

[7] C. Pramanik, J. R. Gissinger, S. Kumar, H. Heinz, *ACS Nano* **2017**, *11*, 12805.

[8] J. H. Koo, J.-K. Song, D.-H. Kim, *Nanotechnology* **2019**, *30*, 132001.

[9] J. H. Koo, S. Jeong, H. J. Shim, D. Son, J. Kim, D. C. Kim, S. Choi, J.-I. Hong, D.-H. Kim, *ACS Nano* **2017**, *11*, 10032.

[10] H. Zhang, Y. Liu, C. Yang, L. Xiang, Y. Hu, L.-M. Peng, *Adv. Mater.* **2018**, *30*, 1805408.

[11] E. J. Park, K.-D. Kim, H. S. Yoon, M.-G. Jeong, D. H. Kim, D. Chan Lim, Y. H. Kim, Y. D. Kim, *RSC Adv.* **2014**, *4*, 30368.

[12] D. Janas, K. K. Koziol, *Nanoscale* **2014**, *6*, 3037.

[13] J. E. Cha, S. Y. Kim, S. H. Lee, *Nanomaterials* **2016**, *6*, 182.

[14] S. Jung, J. H. Kim, J. Kim, S. Choi, J. Lee, I. Park, T. Hyeon, D.-H. Kim, *Adv. Mater.* **2014**, *26*, 4825.

[15] J. W. Jo, J. W. Jung, J. U. Lee, W. H. Jo, *ACS Nano* **2010**, *4*, 5382.

[16] S. He, B. Zhang, M. Liu, W. Chen, *RSC Adv.* **2014**, *4*, 49315.

[17] C. Cao, Y. Zhou, S. Ubnoske, J. Zang, Y. Cao, P. Henry, C. B. Parker, J. T. Glass, *Adv. Energy Mater.* **2019**, *9*, 1900618.

[18] C. Silvestri, M. Riccio, R. H. Poelma, A. Jovic, B. Morana, S. Vollebregt, A. Irace, G. Q. Zhang, P. M. Sarro, *Small* **2018**, *14*, 1800614.

[19] E. R. Meshot, D. L. Plata, S. Tawfick, Y. Zhang, E. A. Verploegen, A. J. Hart, *ACS Nano* **2009**, *3*, 2477.

[20] C. Choi, M. K. Choi, S. Liu, M. S. Kim, O. K. Park, C. Im, J. Kim, X. Qin, G. J. Lee, K. W. Cho, M. Kim, E. Joh, J. Lee, D. Son, S.-H. Kwon, N. L. Jeon, Y. M. Song, N. Lu, D.-H. Kim, *Nat. Commun.* **2017**, *8*, 1664.

[21] Y. Li, H. Zhang, Y. Yao, T. Li, Y. Zhang, Q. Li, Z. Dai, *RSC Adv.* **2015**, *5*, 46749.

[22] M. Wang, T. Li, Y. Yao, H. Lu, Q. Li, M. Chen, Q. Li, *J. Am. Chem. Soc.* **2014**, *136*, 18156.

[23] S. Hong, J. Lee, K. Do, M. Lee, J. H. Kim, S. Lee, D.-H. Kim, *Adv. Funct. Mater.* **2017**, *27*, 1704353.

[24] C. H. Lee, J.-H. Kim, C. Zou, I. S. Cho, J. M. Weisse, W. Nemeth, Q. Wang, A. C. T. van Duin, T.-S. Kim, X. Zheng, *Sci. Rep.* **2013**, *3*, 2917.

[25] B. Le Borgne, S. Liu, X. Morvan, S. Crand, R. A. Sporea, N. Lu, M. Harnois, *Adv. Mater. Technol.* **2019**, *4*, 1800600.

[26] N. Muralidharan, E. Teblum, A. S. Westover, D. Schauben, A. Itzhak, M. Muallem, G. D. Nessim, C. L. Pint, *Sci. Rep.* **2018**, *8*, 17662.

[27] G. Lee, J. W. Kim, H. Park, J. Y. Lee, H. Lee, C. Song, S. W. Jin, K. Keum, C.-H. Lee, J. S. Ha, *ACS Nano* **2019**, *13*, 855.

[28] D.-H. Kim, W. M. Choi, J.-H. Ahn, H.-S. Kim, J. Song, Y. Huang, Z. Liu, C. Lu, C. G. Koh, J. A. Rogers, *Appl. Phys. Lett.* **2008**, *93*, 044102.

[29] T. Li, Z. Suo, S. P. Lacour, S. Wagner, *J. Mater. Res.* **2005**, *20*, 3274.

[30] B. Zhang, J. Lei, D. Qi, Z. Liu, Y. Wang, G. Xiao, J. Wu, W. Zhang, F. Huo, X. Chen, *Adv. Funct. Mater.* **2018**, *28*, 1801683.

[31] Z. Lv, Y. Tang, Z. Zhu, J. Wei, W. Li, H. Xia, Y. Jiang, Z. Liu, Y. Luo, X. Ge, Y. Zhang, R. Wang, W. Zhang, X. J. Loh, X. Chen, *Adv. Mater.* **2018**, *30*, 1805468.

[32] C. Yang, H. Zhang, Y. Liu, Z. Yu, X. Wei, Y. Hu, *Adv. Sci.* **2018**, *5*, 1801070.

[33] B. Zhang, J. Liang, C. L. Xu, B. Q. Wei, D. B. Ruan, D. H. Wu, *Mater. Lett.* **2001**, *51*, 539.

[34] S. F. Cogan, P. R. Troyk, J. Ehrlich, T. D. Plante, *IEEE Trans. Biomed. Eng.* **2005**, *52*, 1612.

[35] W. Chen, R. B. Rakhi, L. Hu, X. Xie, Y. Cui, H. N. Alshareef, *Nano Lett.* **2011**, *11*, 5165.

[36] L. Dong, C. Xu, Y. Li, Z. Pan, G. Liang, E. Zhou, F. Kang, Q.-H. Yang, *Adv. Mater.* **2016**, *28*, 9313.

[37] L. Hu, M. Pasta, F. La Mantia, L. Cui, S. Jeong, H. D. Deshazer, J. W. Choi, S. M. Han, Y. Cui, *Nano Lett.* **2010**, *10*, 708.

[38] Y. Jiang, X. Cui, L. Zu, Z. Hu, J. Gan, H. Lian, Y. Liu, G. Xing, *Nano-materials* **2015**, *5*, 1638.

[39] D. N. Futaba, K. Hata, T. Yamada, T. Hiraoka, Y. Hayamizu, Y. Kakudate, O. Tanaike, H. Hatori, M. Yumura, S. Iijima, *Nat. Mater.* **2006**, *5*, 987.

[40] S. Jung, J. Lee, T. Hyeon, M. Lee, D.-H. Kim, *Adv. Mater.* **2014**, *26*, 6329.

[41] Y. Lei, W. Zhao, Y. Zhang, Q. Jiang, J.-H. He, A. J. Baeumner, O. S. Wolfbeis, Z. L. Wang, K. N. Salama, H. N. Alshareef, *Small* **2019**, *15*, 1901190.

[42] S. H. Kim, S. Jung, I. S. Yoon, C. Lee, Y. Oh, J.-M. Hong, *Adv. Mater.* **2018**, *30*, 1800109.

[43] M. K. Kim, R. N. Parasuraman, L. Wang, Y. Park, B. Kim, S. J. Lee, N. Lu, B.-C. Min, C. H. Lee, *NPG Asia Mater.* **2019**, *11*, 43.

[44] B.-U. Hwang, A. Zabeeb, T. Q. Trung, L. Wen, J. D. Lee, Y.-I. Choi, H.-B. Lee, J. H. Kim, J. G. Han, N.-E. Lee, *NPG Asia Mater.* **2019**, *11*, 23.

[45] Y. R. Jeong, G. Lee, H. Park, J. S. Ha, *Acc. Chem. Res.* **2019**, *52*, 91.

[46] S. Hong, S. Lee, D. Kim, *Proc. IEEE* **2019**, *107*, 2185.

[47] S. Ahn, A. Choe, J. Park, H. Kim, J. G. Son, S.-S. Lee, M. Park, H. Ko, *J. Mater. Chem. C* **2015**, *3*, 2319.

[48] S. Choi, S. I. Han, D. Jung, H. J. Hwang, C. Lim, S. Bae, O. K. Park, C. M. Tschabrunn, M. Lee, S. Y. Bae, J. W. Yu, J. H. Ryu, S.-W. Lee, K. Park, P. M. Kang, W. B. Lee, R. Nezafat, T. Hyeon, D.-H. Kim, *Nat. Nanotechnol.* **2018**, *13*, 1048.